

Fast Robust Methods for Singular State-Space Models

Jonathan Jonker^{1,a}, Aleksandr Aravkin^b, James Burke^a, Gianluigi Pillonetto^d,
Sarah Webster^c.

^a*Department of Mathematics, University of Washington*

^b*Department of Applied Mathematics, University of Washington*

^c*Applied Physics Lab, University of Washington*

^d*Department of Information Engineering, University of Padova*

Abstract

State-space models are used in a wide range of time series analysis applications. Kalman filtering and smoothing are work-horse algorithms in these settings. While classic algorithms assume Gaussian errors to simplify estimation, recent advances use a broad range of optimization formulations to allow outlier-robust estimation, as well as constraints to capture prior information.

Here we develop methods on state-space models where either transition or error covariances may be singular. These models frequently arise in navigation (e.g. for ‘colored noise’ models or deterministic integrals) and are ubiquitous in auto-correlated time series models such as ARMA. We reformulate all state-space models (singular as well as nonsingular) as constrained convex optimization problems, and develop an efficient algorithm for this reformulation. The convergence rate is *locally linear*, with constants that do not depend on the conditioning of the problem.

Numerical comparisons show that the new approach outperforms competing approaches for *nonsingular* models, including state of the art interior point (IP) methods. IP methods converge at superlinear rates; we expect them to dominate. However, the steep rate of the proposed approach (independent of problem conditioning) combined with cheap iterations wins against IP in a run-time comparison. This suggests that the proposed approach can be a *default choice* for estimating state space models outside of the Gaussian context for singular and nonsingular models. To highlight the capabilities of the new framework, we focus on navigation applications that use singular process covariance models, and analyze data from a drifting mooring as a proxy for an autonomous underwater vehicle.

1 Introduction

The linear state space model is widely used in tracking and navigation [8], control [1], signal processing [2], and other time series [12,22]. The model assumes linear relationships between latent states with noisy observations:

$$\begin{aligned} x_1 &= x_0 + w_1 \\ x_k &= G_k x_{k-1} + w_k, \quad k = 2, \dots, N \\ y_k &= H_k x_k + v_k, \quad k = 1, \dots, N, \end{aligned} \quad (1)$$

where x_0 is a given initial state estimate, x_1, \dots, x_N are unknown latent states with known linear process mod-

els G_k , and y_1, \dots, y_N are observations obtained using known linear models H_k . Data must be in the range of H_k ; so we assume H_k are surjective.

The errors w_k and v_k are assumed to be mutually independent random variables with known covariances Q_k and R_k . In tracking and navigation, the end goal is the estimation of the latent states $\{x_k\}$. In autocorrelated time series models (e.g. Holt-Winters c.f. [12], ARMA c.f. [22]), estimating the state is a necessary step to estimating additional parameters on which G_k , H_k , Q_k and R_k may depend. In both settings, estimating the state sequence $\{x_k\}$ efficiently is essential.

Singular Covariances. We are particularly interested in models where Q_k and R_k may be singular. These models arise in all settings where state-space formulations are used. In navigation, the simplest example is the DC

Email addresses: jonkerjo@uw.edu (Jonathan Jonker), saravkin@uw.edu (Aleksandr Aravkin), jvburke@uw.edu (James Burke), giapi@dei.unipd.it (Gianluigi Pillonetto), swebster@apl.washington.edu (Sarah Webster).

¹ The views, opinions and/or findings expressed are those of the authors and should not be interpreted as representing the official views or policies of the Department of Defense or the U.S. Government.

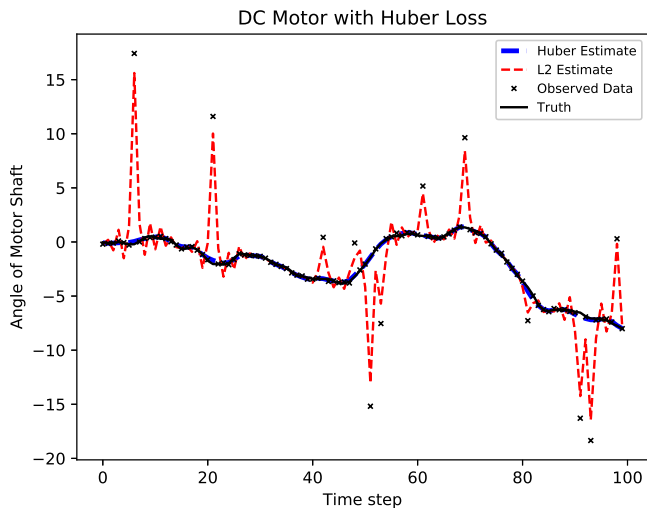


Fig. 1. DC motor (2) with outliers, generated from a Gaussian with high variance. The process covariance Q is singular, but the standard RTS smoother still finds the linear minimum variance estimate (red). Our reformulation allows using robust penalties (in this case, Huber) with a singular covariances to obtain a better solution (blue).

motor [16, pp. 95-97]:

$$\begin{aligned} x_{k+1} &= \begin{pmatrix} 0.7 & 0 \\ 0.084 & 1 \end{pmatrix} x_k + \begin{pmatrix} 11.81 \\ 0.62 \end{pmatrix} (c_k + d_k) \\ y_k &= \begin{pmatrix} 0 & 1 \end{pmatrix} x_k + v_k. \end{aligned} \quad (2)$$

Here, y_k are noisy samples of the angle of the motor shaft, c_k are known inputs, and d_k denote random process disturbances. The covariance matrix Q_k associated to w_k has dimension 2 and rank 1. This example is general in the sense that singular models appear any time a single source of error is integrated into multiple states; a pervasive phenomenon in navigation models [2].

The classic Kalman filter [14] and RTS smoother [20] assume that w_k, v_k are Gaussian, and find the minimum variance estimates of the state, conditioned on the observations [2]. More generally, the RTS smoother finds the linear minimum variance estimator. This procedure is well defined for singular covariances Q_k and R_k , and the smoother can be derived as a sequence of least squares projections [3]. However, when the noise is not Gaussian (e.g. in the presence of outliers), these estimates are not satisfactory; and far better estimates can be obtained through a maximum a posteriori (MAP) estimator [4]. The results in Figure 1 are obtained using the Huber loss, which is a convex penalty function that is quadratic near the origin, but with linear tails:

$$\rho(x) = \begin{cases} \frac{1}{2}x^2 & \text{if } |x| \leq \kappa \\ \kappa(|x| - \frac{1}{2}\kappa) & \text{if } |x| \geq \kappa \end{cases}$$

Implementing a general MAP estimator for singular covariances requires a new approach.

General Kalman Smoothing. Classic Gaussian formulations fail when outliers are present in the data, are unable to track abrupt state changes, and cannot incorporate side information through constraints. To develop effective approaches in these cases, generalized Kalman smoothing formulations have been proposed in the last few years, see [4] and the references within. The conditional mean is no longer tractable to compute these estimates, and *maximum likelihood* (ML) formulations are much more natural. The general form of Kalman smoothing considered in [4] is given by

$$\min_{x \in X} \sum_{i=0}^n \rho_1(Q_k^{-1/2}(x_k - G_k x_{k-1})) + \rho_2(R_k^{-1/2}(y_k - H_k x_k)), \quad (3)$$

where ρ_1, ρ_2 are convex penalties, and $x \in X$ is a set of state-space constraints. The two approaches agree in the nonsingular Gaussian case, where (3) becomes a least squares (LS) problem that can be solved with classic RTS or Mayne-Fraser smoothing algorithms [4].

Contribution. We develop a new reformulation to extend (3) to singular covariance models Q_k and R_k , and implement a Douglas-Rachford splitting (DRS) algorithm to solve this reformulation. The result in Figure 1 uses Huber penalties for process and measurement, with the singular process covariance model from (2).

We analyze the DRS for the singular reformulation, and show that it converges locally linearly for any piecewise linear quadratic (PLQ) loss, and that the rate does not depend on the conditioning of the system. Even when the model is nonsingular, the new approach is potentially much faster than first-order and second-order methods for (3). The advantage increases as the models become more ill-conditioned; however the *local* linear rate means that initialization becomes very important.

The paper proceeds as follows. In Section 2 we discuss prior approaches to singular models. In Section 3, we develop a constrained reformulation of (3), building on early work of [19] for singular least squares. In Section 4, we show how to efficiently optimize a wide range of singular smoothing problems using DRS. The algorithm we use has a *local linear rate of convergence* for any piecewise linear-quadratic penalties ρ_1, ρ_2 in (3), and each iteration is efficiently and stably computed by exploiting dynamic problem structure. We compare the new algorithm to first-order methods, L-BFGS, and IP-solve, a toolbox specifically developed for PLQ Kalman smoothing (for nonsingular formulations). In Section 5, we present a navigation model that uses singular errors. In Section 6 we apply the methodology to analyze data from a drifting mooring as a proxy for an autonomous underwater vehicle.

2 Related Work

Several approaches in the literature deal with singular models. We give a brief description and references for each. To ground the discussion, consider tracking a particle moving along a smooth path in space, where state comprises velocity and position. Singular models arise naturally in this situation. We can model velocity as subject to error, and position as a deterministic integral:

$$\begin{aligned} x_{k+1} &= x_k + \Delta t \dot{x}_k \\ \dot{x}_{k+1} &= \dot{x}_k + \epsilon_k. \end{aligned} \quad (4)$$

Here, the process covariance matrix Q_k has rank one. **Using the original Kalman filter.** In the linear Gaussian setting, the original Kalman filter does not require Q and R to be invertible. Applying the Kalman filter (and RTS smoother) will return the minimum variance estimate for singular innovation/measurement errors [2]. The limitation is that we cannot consider the general optimization context (3), which we need to incorporate robustness to outliers and constraints for prior information (see example in Figure 1).

Changing the model. A common approach is to modify the model to make Q_k, R_k nonsingular. Treating (4) as a discretization of a stochastic differential equation (SDE), many authors opt for a nonsingular error model [13,18,9,7]

$$Q_k = \begin{bmatrix} \Delta t_k & \Delta t_k^2/2 \\ \Delta t_k^2/2 & \Delta t_k^3/3 \end{bmatrix},$$

derived by computing the variance of a discretized process noise term, similar to what is done in Section 5, see (21). The approach has limitations for navigation models with high-dimensional states driven by low-dimensional errors. The low-dimensional error structure should simplify estimation, but instead this approach introduces full-dimensional and ill-conditioned Q_k . In addition, making Q_k nonsingular is antithetical to state-space formulations for models such as ARMA, which use singularity to enforce auto-regressive constraints.

Change of coordinates. When only R_k are singular, [2] suggests making a change of coordinates in the measurement variables and then projecting to remove the extra dimensions. The projections can vary between time points, and the approach does not extend to the singular state equation (4).

Pseudo-inverse with orthogonality constraints. The formulation that is closest to ours is that of [17], who replace the inverse of Q_k by a pseudo-inverse, and add orthogonality constraints (namely that projection onto the null space of Q_k is zero). With potentially singular Q_k and R_k , the maximum likelihood estimate for

the Gaussian/LS model can be formulated as

$$\begin{aligned} \min_x \sum_k & \|Q_k^{\dagger/2}(x_k - G_k x_{k-1})\|^2 + \|R_k^{\dagger/2}(y_k - H_k x_k)\|^2 \\ \text{s.t. } & Q_k^\perp(x_k - G_k x_{k-1}) = 0, \quad R_k^\perp(y_k - H_k x_k) = 0 \\ & \text{for all } k = 1, \dots, N, \end{aligned} \quad (5)$$

see [4, Appendix A]. This requires computing both the pseudo-inverse and orthogonality constraints.

Constrained reformulation. The reformulation we choose was first used by Paige [19]. Given the singular least squares problem

$$\min_x \|Q^{\dagger/2}(Ax - b)\|^2 \quad \text{s.t.} \quad Q^\perp(Ax - b) = 0,$$

we can instead write it as

$$\min_{x,u} \|u\|^2 \quad \text{s.t.} \quad Q^{1/2}u = Ax - b. \quad (6)$$

It is easy to see (5) and (6) are equivalent; the latter is more elegant, and only requires computing a root of Q , rather than using both Q and Q^\dagger . When Q is invertible, we can eliminate u from both formulations and reduce to a least squares problem in x . Splitting the affine constraint from the original penalty has theoretical and practical advantages for general Kalman smoothing, as shown in the next sections.

3 General Singular Kalman Smoothing

Following the ideas proposed by [17], we introduce variables u_k for the normalized process innovations, and t_k for the normalized residuals. We also introduce a penalty ρ_3 for the states. In the examples we consider, ρ_3 is an indicator function for the known feasible regions X_k :

$$\rho_3(x_k) = \begin{cases} 0 & x_k \in X_k \\ \infty & x_k \notin X_k \end{cases}.$$

The reformulated singular Kalman smoothing problem is given by

$$\begin{aligned} \min_{u,t,x} \sum_{k=1}^N & \rho_1(u_k) + \rho_2(t_k) + \rho_3(x_k) \\ \text{s.t. } & Q_k^{1/2}u_k = G_k x_{k-1} - x_k \\ & R_k^{1/2}t_k = y_k - H_k x_k \end{aligned} \quad (7)$$

This problem is equivalent to (3) when Q_k and R_k are nonsingular. For singular models, (7) requires only that roots $Q^{1/2}$ and $R^{1/2}$ are available.

Constrained Robust DC motor. Recall the DC motor example in the introduction (2). The data used to make Figure 1 is contaminated with outliers, so we want

to use the robust Huber loss for the measurement errors. Suppose we also know upper and lower bounds on the states, $B := \{x : l \leq x \leq u\}$. Then the formulation of the robust constrained singular DC motor is given by

$$\min_{u,t,x} \sum_{k=1}^N \|u_k\|^2 + \rho_h(t_k) + \delta_B(x_k), \quad \sigma t_k = a_k - x_{2,k},$$

$$\begin{bmatrix} 11.8 & 0 \\ 0.62 & 0 \end{bmatrix} u_k = x_{k+1} - \begin{pmatrix} 0.7 & 0 \\ 0.084 & 1 \end{pmatrix} x_k - \begin{pmatrix} 11.81 \\ 0.62 \end{pmatrix} c_k.$$

Structure-preserving Reformulation. We now rewrite (7) into a more compact form. Define

$$D_i = \begin{pmatrix} Q_i^{1/2} & 0 & I \\ 0 & R_i^{1/2} & H_i \end{pmatrix} \text{ for } i = 1, \dots, N,$$

$$B_j = \begin{pmatrix} 0 & 0 & -G_{j+1} \\ 0 & 0 & 0 \end{pmatrix}, \text{ for } j = 1, \dots, N-1,$$
(8)

and let

$$A = \begin{pmatrix} D_1 & 0 & \dots & 0 \\ B_1 & D_2 & 0 & \vdots \\ 0 & \ddots & \ddots & 0 \\ 0 & 0 & B_{N-1} & D_N \end{pmatrix}.$$
(9)

Define also

$$z^T = (u_1^T \ t_1^T \ x_1^T \ \dots \ u_N^T \ t_N^T \ x_N^T)$$

$$\hat{w}^T = (x_0^T \ y_1^T \ 0 \ y_2^T \ \dots \ 0 \ y_N^T).$$
(10)

Now we can write (7) compactly as

$$\min_z \rho(z) \quad \text{s.t. } Az = \hat{w},$$

$$\rho(z) = \sum_{k=1}^N \rho_1(u_k) + \rho_2(t_k) + \rho_3(x_k).$$
(11)

The order of blocks in z is chosen to the constraint matrix A in (9) lower block bi-diagonal.

The constraint $Az = \hat{w}$ raises a natural question: when is a singular Kalman smoothing model solvable? Clearly we want $\hat{w} \in \text{Ran}(A)$, but we want this condition to hold for any realization of the data \hat{w} , so we want to know when A is surjective. We can characterize this condition precisely in terms of a simple conditions on the individual blocks R_i, Q_i, H_i .

Theorem 3.1 (Surjectivity of A) *The following are equivalent.*

- (1) A is surjective.
- (2) Each block D_i is surjective.
- (3) $\text{null} \left(\begin{bmatrix} Q_i^{1/2} & 0 \\ 0 & R_i^{1/2} \end{bmatrix} \right) \subset \text{Ran} \left(\begin{bmatrix} I \\ H_i \end{bmatrix} \right)$ for all i .
- (4) $R_i + H_i (I - (Q_i + I)^{-1}) H_i^T$ is invertible for all i .

The proof is given in the Appendix.

4 Douglas-Rachford Splitting for General Singular Kalman Smoothing

Consider problem (11) as a sum of two functions, $\rho + g$, with ρ as in (11) and g the indicator function of the affine constraint $Az = \hat{w}$:

$$g(z) = \begin{cases} 0 & Az = \hat{w} \\ \infty & Az \neq \hat{w} \end{cases}.$$
(12)

Douglas-Rachford splitting (DRS) is a classic algorithm for this problem. For a convex function f , define the proximity operator (see e.g. [10]) as

$$\text{prox}_{\alpha f}(\zeta) = \arg \min_x \frac{1}{2\alpha} \|\zeta - x\|^2 + f(x).$$

The DRS algorithm for (11) detailed in Algorithm 1. For more on splitting methods and their convergence rates see the survey [11].

Algorithm 1 Douglas-Rachford Splitting (DRS)

Require: Initialize at any z^0, ζ^0 .

- 1: **loop**
- 2: $z^k = \text{prox}_{\tau g}(z^{k-1} - \tau \zeta^{k-1})$
- 3: $\zeta^k = \text{prox}_{\sigma \rho^*}(\zeta^{k-1} + \sigma(2z^k - z^{k-1}))$

return z^k

Implementing DRS in our case requires computing two proximity operators at each iteration. One proximity operator is prox_{ρ^*} , where ρ^* denotes the *convex conjugate*:

$$\rho^*(y) = \sup_x \langle y, x \rangle - \rho(x)$$

The prox of of a function is related to the prox of its conjugate by Moreau's decomposition:

$$\text{prox}_{\rho}(x) + \text{prox}_{\rho^*}(x) = x.$$

Thus it suffices to compute prox_{ρ} . The function ρ captures all user-supplied models, including losses used process and measurement transitions, as well as penalties or constraints on the state, ρ_1, ρ_2 and ρ_3 . The proximity operators of these individual elements must be provided; then prox_{ρ} is a stack of these input functions. Proximity operators for many common functions

are easily available [10], and we include a small library with our implementation².

The second proximity operator is prox_g , which is independent of user choice for process, measurement, and prior models:

$$\text{prox}_g(\eta) = \arg \min_{A z = \hat{w}} \frac{1}{2} \|\eta - z\|^2.$$

This is a simple quadratic with affine constraints, with optimality conditions given by

$$\begin{bmatrix} I & A^T \\ A & 0 \end{bmatrix} \begin{bmatrix} z \\ \nu \end{bmatrix} = \begin{bmatrix} \eta \\ \hat{w} \end{bmatrix}.$$

There are many ways to solve this system. We opt to reduce the problem to solving a block tridiagonal system:

$$\begin{bmatrix} I & A^T \\ 0 & AA^T \end{bmatrix} \begin{bmatrix} z \\ \nu \end{bmatrix} = \begin{bmatrix} \eta \\ A\eta - \hat{w} \end{bmatrix}$$

We solve $AA^T \nu = A\eta - \hat{w}$, then back-substitute to get the optimal z . The system AA^T does not change over iterations; only the right hand side changes. We can therefore compute a single factorization, then use it in each iteration. Since A is block bidiagonal (9), AA^T is block tridiagonal; when A is surjective, AA^T is nonsingular, and we can find a lower block diagonal Cholesky factorization L with $LL^T = AA^T$:

$$AA^T = \begin{bmatrix} a_1 & b_1^T & & & \\ b_1 & a_2 & b_2^T & & \\ & b_2 & a_3 & b_3^T & \\ & & b_3 & a_4 & \\ & & & & \end{bmatrix}, \quad L = \begin{bmatrix} c_1 & & & & \\ d_1 & c_2 & & & \\ & d_2 & c_3 & & \\ & & d_3 & c_4 & \\ & & & & \end{bmatrix} \quad (13)$$

The factorization is detailed in Algorithm 2.

Algorithm 2 Block bi-diagonal Cholesky factorization for a block tri-diagonal positive definite matrix

Require: Input block diagonals $\{a_i\}$ and lower off-diagonals $\{b_i\}$ of block tridiagonal matrix AA^T (13).

- 1: $s_0 = 0, b_0 = 0$
- 2: **loop** $k = 1, \dots, N$
- 3: $s_k = a_k - b_{k-1} s_{k-1}^{-1} b_{k-1}^T$
- 4: $c_k = \text{chol}(s_k)$
- 5: $d_k = b_1 c_k^{-T}$

return Diagonal blocks $\{c_i\}$ and lower-diagonal blocks d_i of block L (13)

Algorithm 2 is derived as follows. Multiplying out LL^T we have

$$a_1 = c_1 c_1^T, \quad d_1 = b_1 c_1^{-T}$$

² <https://github.com/UW-AMO/KalmanJulia>.

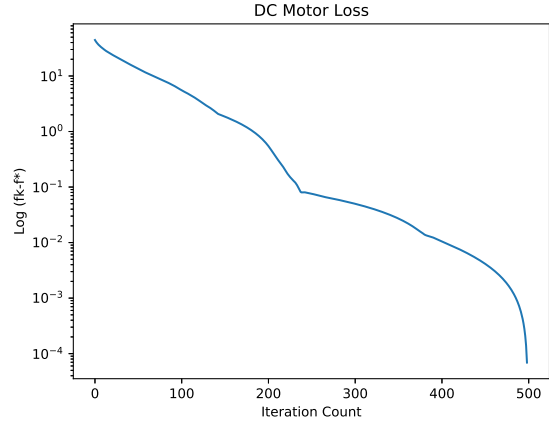


Fig. 2. Convergence rate for DRS splitting is locally linear when the objectives are piecewise linear-quadratic (PLQ). The convergence plot show here corresponds to the robust DC motor example in Figure 1.

To compute c_1 we need the standard the Cholesky factorization of a_1 . Then

$$c_2 c_2^T = a_2 - b_1 a_1^{-1} b_1^T, \quad d_2 = b_2 c_2^{-1}.$$

For convenience, we introduce the recursively defined auxiliary terms s_k , with $s_1 = a_1$, and

$$s_k = a_k - b_{k-1} s_{k-1}^{-1} b_{k-1}^T.$$

Then each c_k is the standard Cholesky factorization of s_k , and d_k is immediately computed as in Algorithm 2. The overall complexity required for the single factorization is $O(n^3 N)$. Once L has been pre-computed, we need only $O(n^2 N)$ arithmetic operations to solve $LL^T \nu = Ac - \hat{w}$ for any right hand side. This is the same complexity as that of a matrix-vector multiply with A .

Local Linear Rate. When ρ is piecewise linear-quadratic [21,5], the DRS algorithm converges locally linearly to a solution, see Figure 2. More precisely, there is a real number $R > 0$ such that if $\|\eta^K - \eta^*\| < R$ then there is a constant κ with $0 < \kappa < 1$ such that for all $k > K$,

$$\|\eta^{k+1} - \eta^*\| < \kappa \|\eta^k - \eta^*\|,$$

where $\eta = \begin{bmatrix} z \\ \zeta \end{bmatrix}^T$, is the primal and dual pair.

Theorem 4.1 Algorithm 1 converges with a locally linear rate.

Proof: Following the proof technique of [15, Theorem 5], Algorithm 1 has a local linear convergence rate if the following two conditions are satisfied:

- (1) Algorithm 1 can be written as the action of a non-linear operator satisfying a regularity property (see Lemma 4.2).

(2) The functions g, ρ are *subdifferentially metrically subregular*³.

We show that these conditions hold for Algorithm 1. Define

$$Dx \mapsto \begin{bmatrix} \partial g(z) \\ \partial \rho^*(\zeta) \end{bmatrix}, \quad M = \begin{bmatrix} 0 & I \\ -I & 0 \end{bmatrix}, \quad H = \begin{bmatrix} \frac{1}{\tau} I & 0 \\ -2I & \frac{1}{\sigma} I \end{bmatrix}.$$

Define the nonlinear operator T by

$$T = (H + D)^{-1}(H - M). \quad (14)$$

T captures the iteration in Algorithm 1, which can be written as $\eta^k = T\eta^{k-1}$, for $\eta = [z^T, \zeta^T]^T$. Then we have the following lemma.

Lemma 4.2 *Suppose that $\tau, \sigma < 1$. Then*

$$\|T\eta - \eta\|_{H-M}^2 \leq \langle \eta^* - \eta, (H - M)(T\eta - \eta) \rangle$$

where η^* is such that $0 \in (D + M)\eta^*$.

The proof is given in the Appendix.

This establishes condition (1). Condition (2) requires the concept of metric subregularity. This property holds for PLQ functions [15], and holds for indicators of convex sets by [6, Theorem 3.3], reproduced in the Appendix. This completes the proof of the theorem.

Comparison on Smooth Nonsingular Problems. If the covariances, Q, R are non-singular and the penalties $\rho_{1,2}$ are \mathcal{C}^1 -smooth, then the Kalman smoothing problem can be written as a smooth convex problem. In this case the same reformulation will work and Algorithm 1 will still give a local linear rate. However more common algorithms such as gradient descent and L-BFGS can also be applied. We compare the performance of these three algorithms to track a particle moving along a smooth path with $N = 200$ and $n = 2$. We use nonsingular Q_k , and Huber penalty functions.

As seen in Figure 3, Algorithm 1 for (11) converges far faster than either accelerated gradient descent or LBFGS method on the equivalent nonsingular smoothing formulation (3). This is because its convergence rate does not depend on the condition number of the matrix A , so each iteration makes a lot of progress, and we can keep the complexity of each iteration at $O(n^2N)$, same

³ A mapping $F : \mathbb{R}^n \rightrightarrows \mathbb{R}^m$ is called *metrically subregular* at \bar{x} for \bar{y} if $(\bar{x}, \bar{y}) \in \text{graph } F$ and there exists $\eta \in [0, \infty)$, neighborhoods \mathcal{U} of \bar{x} , and \mathcal{Y} of \bar{y} such that

$$d(x, F^{-1}\bar{y}) \leq \eta d(\bar{y}, Fx \cap \mathcal{Y}), \quad \forall x \in \mathcal{U}$$

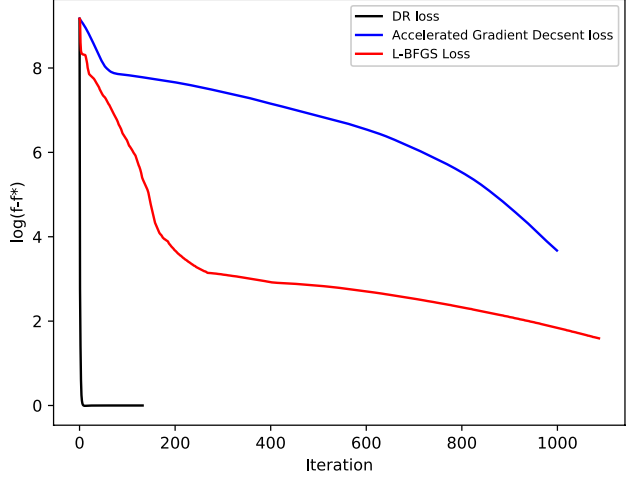


Fig. 3. Objective vs. iteration counts of Algorithm 1 for (11) (black), vs. accelerated gradient descent (AGD) (blue) and L-BFGS (red) for (3). Both ρ_1 and ρ_2 are Huber losses, with $\rho_3 \equiv 0$, $N = 200$, $n = 2$ and Q, R nonsingular, so (11) and (3) are equivalent. All iterations require $O(n^2N)$ operations. DRS splitting is much faster than methods with linear convergence rates and similar iteration complexity.

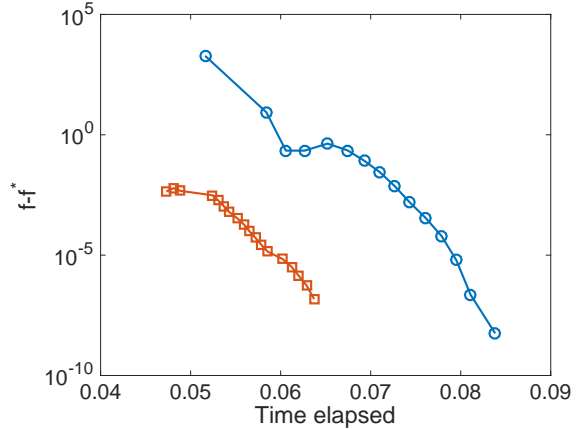


Fig. 4. Timed run of Algorithm 1 vs. IPsolve for the same setup as presented in Figure 3. At this scale, we see the locally linear convergence rate of the DRS. Even though IPsolve has superlinear rate, DRS wins because the slope of the rate is very steep, and each iteration is fast. By the time DRS is done, IPsolve has had time for only taken a few iterations.

as for a matrix-vector multiply needed for a gradient evaluation, if we factor the sparse block tridiagonal matrix AA^T once at the start of the algorithm.

We also compare with the second-order interior point method, implemented in the IPsolve package⁴. Use-cases and performance of IPsolve for nonsingular Kalman smoothing is discussed in [4]. The results are shown in Figure 4, where IPsolve and DRS for the equivalent reformulation are compared for the nonsin-

⁴ <https://github.com/UW-AMO/IPsolve>.

gular Huber model. Even though DRS has at best a linear rate, the constants are very good, as they do not depend on the conditioning of the Kalman smoothing problem. The other advantage is that DRS can use a pre-factorized matrix, while IPSolve has to solve a modified linear system every time; there is no simple strategy to pre-factor as with DRS.

The numerical experiments suggest that Algorithm 1 should be used regardless of whether Q and R are singular or not. In the next section, we focus on a rich class of singular noise models found in navigation.

5 Navigation Models

Autonomous navigation requires high-fidelity tracking using occasional GPS and frequent depth/height, gyro-compass, and linear acceleration data. Gyro, compass, and linear acceleration are readily available from inertial measurement units (IMUs).

In this section, we develop a simple kinematic model that is trivially applicable to any vehicle, and is particularly appropriate for many underwater vehicle applications, where accelerations are heavily damped and autonomous vehicles often travel in long straight lines (e.g. for survey work). When the attitude is known or changing slowly, the model can be linearized effectively and the situation simplifies considerably; our synthetic examples and underwater survey application use linearized models.

Linear Singular Navigation Model. For a vehicle that is well-instrumented in attitude, the uncertainty in position (and the x-y states in particular) is typically orders of magnitude larger than the uncertainty in attitude. In practice, we simplify the full nonlinear vehicle process model to track only position states (x, y, z) , while assuming that the attitude states (r, p, h) are directly available from the most recent sensor measurements. To make the model linear, the position and its derivatives are referenced to the local-level frame.

To incorporate linear acceleration measurements from an inertial measurement unit (IMU), we must track both linear velocities and linear acceleration in the state vector. This leads to the augmented state

$$x_s = [x, y, z, \dot{x}, \dot{y}, \dot{z}, \ddot{x}, \ddot{y}, \ddot{z}]^\top. \quad (15)$$

The linear kinematic process model is given by

$$\dot{x}_s = \underbrace{\begin{bmatrix} 0 & I & 0 \\ 0 & 0 & I \\ 0 & 0 & 0 \end{bmatrix}}_{F_s} x_s + \underbrace{\begin{bmatrix} 0 \\ I \\ 0 \end{bmatrix}}_{G_s} w_s, \quad (16)$$

where $w_s \sim \mathcal{N}(0, Q_s)$ is zero-mean Gaussian noise. The linear process model (16) is usually discretized using

a Taylor series:

$$x_{s_{k+1}} = F_{s_k} x_{s_k} + w_{s_k} \quad (17)$$

$$F_{s_k} = e^{F_s T} \quad (18)$$

$$\begin{aligned} &= I + F_s T + \frac{1}{2!} F_s^2 T^2 + \frac{1}{3!} F_s^3 T^3 + \dots \\ &= \begin{bmatrix} I & IT & \frac{1}{2} IT^2 \\ 0 & I & IT \\ 0 & 0 & I \end{bmatrix} \end{aligned}$$

where the higher order terms are *identically zero* because of the structure of F_s , resulting in a simple closed-form solution for F_{s_k} . The discretized process noise

$$w_{s_k} = \int_0^T e^{F_s(T-\tau)} G_s w_s(\tau) d\tau, \quad (19)$$

is a zero-mean Gaussian, with covariance given by

$$Q_{s_k} = \int_0^T e^{F(T-\tau)} G Q G^\top e^{F^\top(T-\tau)} d\tau, \quad (20)$$

which simplifies to

$$Q_{s_k} = \begin{bmatrix} \frac{1}{3} T^3 & \frac{1}{2} T^2 & 0 \\ \frac{1}{2} T^2 & T & 0 \\ 0 & 0 & 0 \end{bmatrix} Q_s, \quad (21)$$

for

$$e^{F(T-\tau)} = \begin{bmatrix} I & I(T-\tau) & \frac{1}{2} I(T-\tau)^2 \\ 0 & I & I(T-\tau) \\ 0 & 0 & I \end{bmatrix}, \quad G = \begin{bmatrix} 0 \\ I \\ 0 \end{bmatrix}.$$

In practice this can lead to wildly incorrect results. In Figure 5, we show the estimate of position obtained from a subset of the navigation data. The model is defined with constraints

$$Q_{s_k}^{1/2} u_{s_k} = F_{s_k} x_{s_{k+1}} - x_{s_k}.$$

The Q in (21) forces the acceleration to be 0 across the entire model because the lower right corner is set to 0. As a result, the initialized track can be biased away from the data by a fixed velocity, obtained by finding the slope from the most recent position data. The available data do not agree, but the constraint is stronger; the information is integrated in a counter-intuitive way.

Instead, we model the covariance as if the error were the

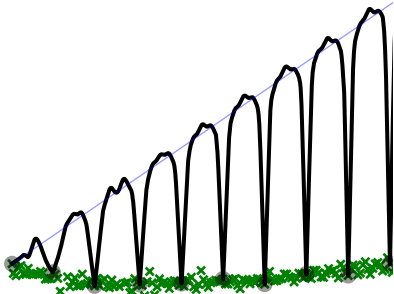


Fig. 5. Full position data is plotted using green crosses; the smoother only uses a subset highlighted with gray disks. The model is used to provide the initialization for the solver, shown in blue, by forward propagating from the first data point. With Q as in (21), the model forces a zero acceleration constraint. Combined with a non-zero initial velocity, this results in an erroneous initialization, which even high confidence in the observed datapoints is unable to overcome, yielding a counterintuitive result.

next term in the Taylor series approximation, a technique suggested by [7]. More precisely we set covariance to be the outer product, $\Gamma^T \Gamma$ where

$$\Gamma = \begin{bmatrix} \frac{1}{3!} IT^3 & \frac{1}{2!} IT^2 & IT \end{bmatrix}$$

This leads to a rank 3 covariance for a 9×9 matrix for a model that comprises position, velocity, and acceleration in 3D space. This model avoids the issue in Figure 5. **Measurement Models for the IMU.** The inertial measurement unit (IMU) does not measure position or velocity, just linear and angular accelerations. To use these measurements, we track linear acceleration as part of the state. However, the acceleration measured by the IMU is relative to the physical frame of the vehicle on which it is mounted, while the acceleration of the state is relative to the navigation frame. A coordinate transformation between these frames is required for a comparison; we use heading, pitch, and roll of the vehicle for the linear model. The transformation from body-frame to local-level is given by $R(\varphi)$, where φ comprises heading h , pitch p , and roll r :

$$R(\varphi) = R_h^T R_p^T R_r^T, \quad (22)$$

where R_h , R_p , and R_r are given by

$$\begin{bmatrix} ch & sh & 0 \\ -sh & ch & 0 \\ 0 & 0 & 1 \end{bmatrix}, \quad \begin{bmatrix} cp & 0 & -sp \\ 0 & 1 & 0 \\ sp & 0 & cp \end{bmatrix}, \quad \begin{bmatrix} 1 & 0 & 0 \\ 0 & cr & sr \\ 0 & -sr & cr \end{bmatrix} \quad (23)$$

with c and s shorthand for $\cos(\cdot)$ and $\sin(\cdot)$.

Any navigation system that relies on an IMU needs occasional measurements that inform the position (e.g. GPS), otherwise the error in position estimates grows without bound. We are given these data from a separate

source, sampled at a lower update rate than that of the IMU. For any s where such data is available, we have the measurement model

$$H_s = \begin{bmatrix} I_{3 \times 3} & 0_{3 \times 6} \\ 0_{3 \times 6} & R(\varphi) \end{bmatrix}, \quad z_s = \begin{bmatrix} b^T & \ddot{x}_{\text{meas}} & \ddot{y}_{\text{meas}} & \ddot{z}_{\text{meas}} \end{bmatrix}^T.$$

If there is no position data measured at time s then we use the model

$$H_s = \begin{bmatrix} 0_{3 \times 3} & 0_{3 \times 6} \\ 0_{3 \times 6} & R(\varphi) \end{bmatrix}, \quad z_s = \begin{bmatrix} 0 & \ddot{x}_{\text{meas}} & \ddot{y}_{\text{meas}} & \ddot{z}_{\text{meas}} \end{bmatrix}^T.$$

The covariance used for measurement data depends on whether there was position data available:

$$R_s = \begin{bmatrix} 0_{3 \times 3} & 0_{3 \times 3} \\ 0_{3 \times 3} & r_s I_{3 \times 3} \end{bmatrix}, \quad R_s = \begin{bmatrix} U_s & 0_{3 \times 3} \\ 0_{3 \times 3} & r_s I_{3 \times 3} \end{bmatrix}$$

where the top 3×3 block is either 0 (position not available) or U , a diagonal matrix reflecting position uncertainty (position is available). The scalar r_s models uncertainty in IMU measurements.

6 Analysis of Mooring Data

We are interested in the ability to maintain an accurate position estimate on-board an autonomous underwater vehicle using acceleration measurements from a low cost inertial measurement unit (IMU), given periodic position fixes. To test this, we use the singular general Kalman framework to analyze data collected from a surface mooring equipped with an IMU that was deployed off the coast of Florida during spring 2017. We use the mooring, which is drifting with the current, as a proxy for a slowly moving underwater vehicle subject to unknown disturbances. In particular we are looking at the position uncertainty and error accrued over time between the periodic, world-referenced position fixes that are provided by the ultra short baseline (USBL) system.

The new capabilities are useful because

- (1) Navigation models are singular
- (2) Data are noisy
- (3) IMU has biases, captured using singular models
- (4) data can be quantized, motivating a special loss.

In this analysis, we use the singular linear kinematics model in Section 5, the Huber loss from Section 1, and the DRS algorithm from Section 4 to solve the final smoothing problem.

6.1 Experimental Setup

As shown in Figure 6, the mooring comprises an articulated spar buoy on the surface, supporting a cable with various instruments attached. The mooring can be shortened using yale grips shown in figure. We are using a portion of data from when the mooring is at its max length of approximately 715m. At 121 meters above

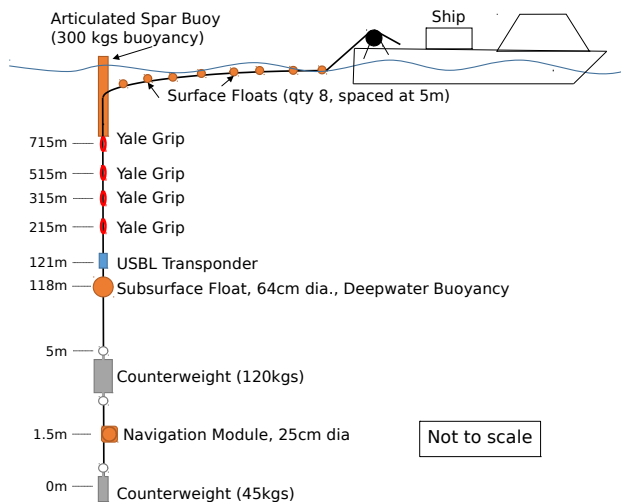


Fig. 6. Sketch of the mooring and tender ship showing major buoyancy and counterweight components and their relative depths. The USBL system provides position fixes of the USBL transponder. The navigation module provides roll, pitch, heading, and linear accelerations.

the bottom of the mooring is an ultra short baseline (USBL) receiver which, in concert with a nearby tender ship, provided three dimensional position updates for the mooring (latitude, longitude, and depth). Below the main clump weight is a 4.25 meter section of Spectra® line with its own smaller clump weight of approximately 45 kg. This supports a 25 cm diameter spherical glass housing containing the navigation module.

The self-contained navigation module, shown in Figure



Fig. 7. The navigation module, housed in a 25 cm diameter glass sphere.

7, consists of a RaspberryPi-based logger supporting a

precision clock (Adafruit ChronoDot RTC v2.1, based on the DS3231 temperature compensated crystal oscillator), gyro (L3GD20H), and accelerometer and compass (LSM303D). The navigation module carries its own batteries and recorded continuously throughout the deployment, providing the time-stamped attitude and acceleration data used in this analysis. Quantization in the attitude (roll, pitch, and yaw) and linear acceleration measurements resulted in a degradation of the native accuracy of the sensors. Table 1 provides a summary of the measurements and associated resolutions as recorded during this experiment. In this capacity the navigation module data serves as a proxy for a low cost autonomous underwater vehicle using a low grade commercial IMU.

Measurement	Resolution	Sample Freq.
time	3.5 ppm	n/a
roll, pitch, yaw	0.1°	25 Hz
lin. acceleration	0.00766 m/s ²	25 Hz

Table 1
Navigation module sensor specifications.

The articulated spar buoy was tethered to the ship through an umbilical that supplied power, two way communications and data transfer. During operations, the intent was to decouple the motion of the ship from that of the surface mooring, keeping slack in this umbilical. This is accomplished by using the ship to tow the mooring into position and then allowing both the ship and mooring to drift with the current.

Ground truth for the position of the mooring was provided by the Sonardyne Ranger 2, a USBL system that provided 3-D position fixes every 2 seconds. The USBL system self reports its measurement uncertainties at each measurement. These ranged from 3.7 to 7.5 m uncertainty in x and y, and 0.8 to 4.0 m uncertainty in depth.

6.2 Model and Experimental Results

Two challenges in the experimental setup required the flexibility of the modeling framework. The depth acceleration data, some of which is plotted in Figure 8, is extremely discretized and appears to have mean shifted away from zero. To counteract this, a constant bias for acceleration measurements was fit and removed. In the singular framework, we easily include a constant term, by imposing equality constraints across all time points using the process model. The measurement maps are then modified to directly subtract the estimated bias. Because of the level of discretization we want to use the Vapnik loss function (Figure 9) that does not penalize in a small interval around the data. The ‘deadzone’ region is set according to the quantization of the data, which is .05. The ‘corners’ of the Vapnik encourage the errors to be exactly equal to the quantization value, an unnecessary artifact. We therefore use a Huberized version of the Vapnik, smoothing the corners but leaving

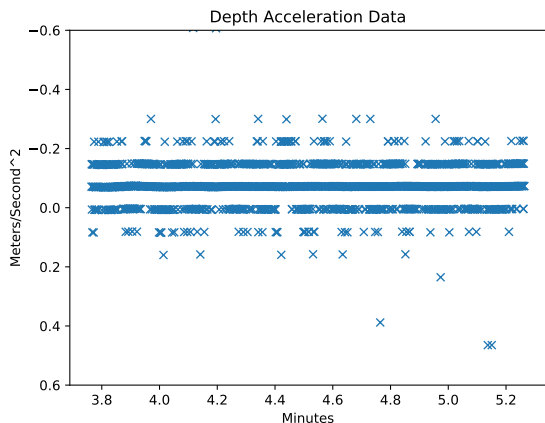


Fig. 8. A snippet of the depth acceleration data, rotated into the world frame, shows the quantization of the acceleration data.

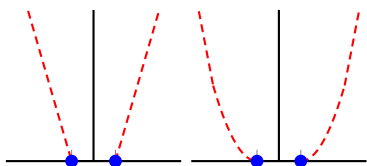


Fig. 9. Vapnik loss function and a smoothed variant.

the deadzone. In addition to the deadzone, this loss is robust, as it has linear tail growth.

Results for 10 Minute Track: We begin by considering 10 minutes of IMU data with occasional USBL position data. The position data are available approximately every 2 seconds, but we test performance with intervals of 30, 60, 120 seconds. The x_0 given to the algorithm is as follows: position is set to the first position fix and acceleration is set to zero, while velocity is taken to be the slope from the last available position data to the starting time. The algorithm is initialized by propagating this x_0 through the entire model and then run for 500 iterations.

Figure 10 shows the depth acceleration data after the bias is removed, now centered around 0. Biases computed for 30, 60, and 120 second intervals were all near 0.073. Figure 11 has the fitted position plots for all three frequencies. The depth plot shows why using only acceleration data is can lead to large errors; small errors in acceleration data build up to have a large effect over time. However when the acceleration data is combined with a small amount of position data all three perform very well. In fact there is not a large difference in the estimates produced; this gives a promising view toward an online implementation. Figure 12 shows the fitted velocity for all three models. Here the small differences in the fit become apparent with lower frequency position data leading to much larger changes in velocity over time.

Results for 50 Minute Track At this scale, we con-

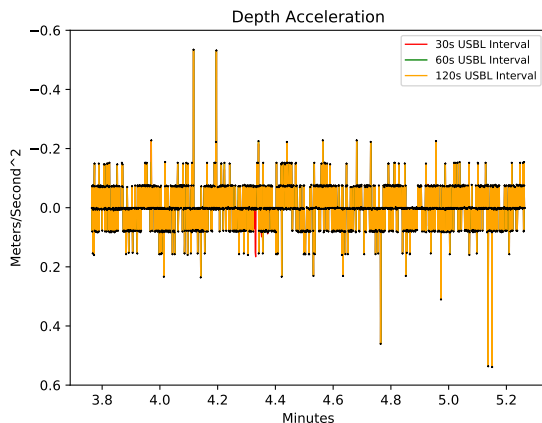


Fig. 10. Depth acceleration data and fit after debiasing.

sider position data at intervals of 3 and 5 minutes. There is also a gap in the position data near minute 27. Figure 13 shows the position estimates for the longer time period. When the position data is only seen every 5 minutes the estimate becomes unstable, especially for depth, where the acceleration data quality is poorest. However even with three minute gaps in between position data the model performs fairly well. Modern underwater vehicles are well-instrumented in depth, and typically have some model for velocity (e.g. hydrodynamic velocity model in gliders, prop counts in propeller-drive vehicles); an extension of the methods proposed here could enable an online navigation system that requires ever fewer high-fidelity external position fixes (such as those provided here from the USBL data).

7 Discussion

We propose a singular Kalman smoothing framework that can use singular covariance models for process and measurements, convex robust losses, and state-space constraints. The modeler can use any convex loss that has an implementable prox; in particular any piecewise linear-quadratic loss and simple polyhedral constraint can be used. The framework offers a range of tools that we illustrated using a sea survey analysis. Future work will consider real-time implementation, as well as extension to nonlinear models.

Numerical experiments illustrate that the local linear rate we have in theory requires a good initialization in practice. All experiments in the paper were initialized by propagating the state estimate forward; this worked far better than an arbitrary initialization (e.g. at the 0 vector). Smarter initialization can be developed for streaming/online contexts, where recent estimates play a key role in initializing smoothing subproblems.

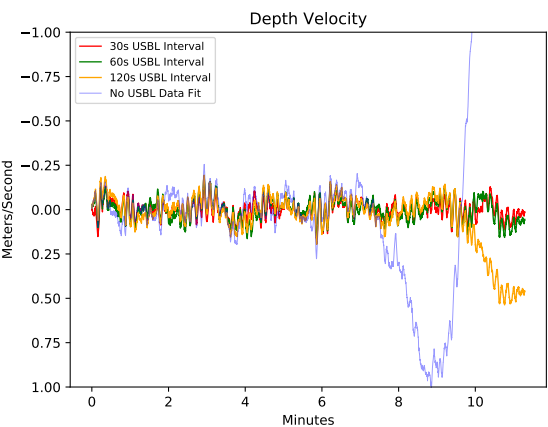
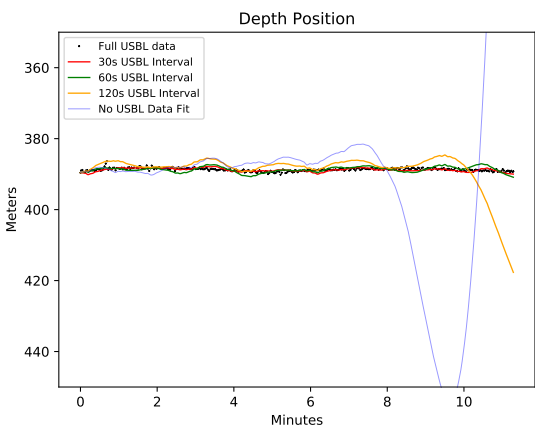
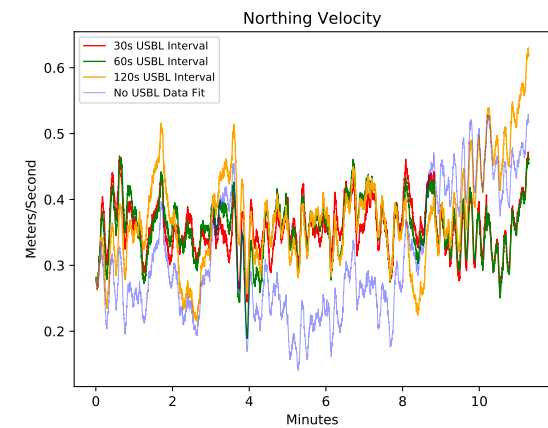
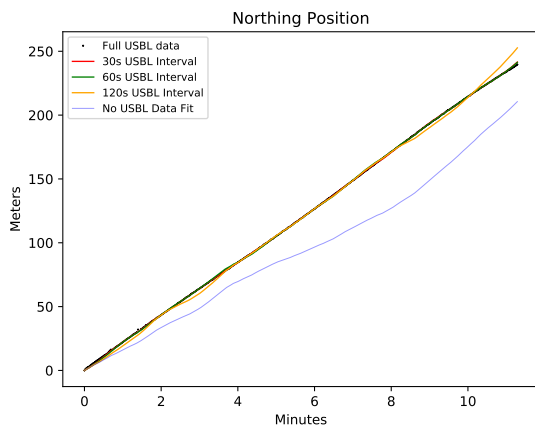
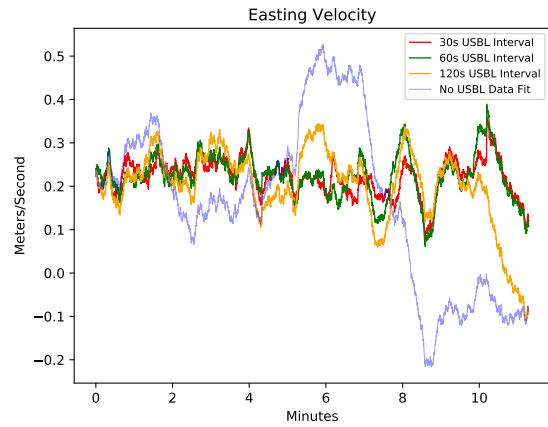
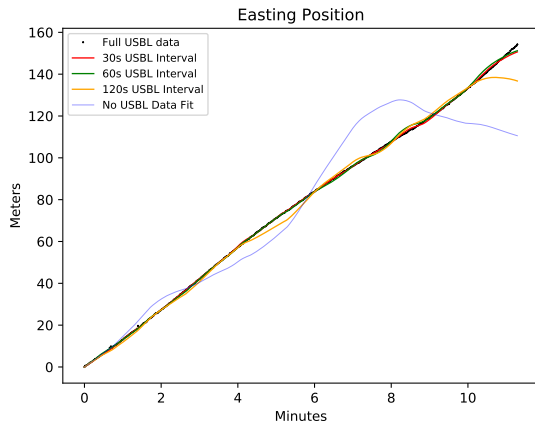


Fig. 11. Fitted position for three frequencies of position data. With supplemental position data the estimates perform much better than when only acceleration data is used.

8 Acknowledgements

This material is based upon work supported by the Defense Advanced Research Agency (DARPA) and Space and Naval Warfare Systems Center Pacific (SSC Pacific) under Contract No. N66001-16-C-4001. The work of Dr. Aravkin was supported by the Washington Re-

Fig. 12. Velocity fit for different frequencies of position data. The build up of acceleration errors can be seen clearly here, especially when no position data is used.

search Foundation Data Science Professorship.

References

- [1] B. D. Anderson and J. B. Moore. *Optimal control: linear quadratic methods*. Courier Corporation, 2007. 1

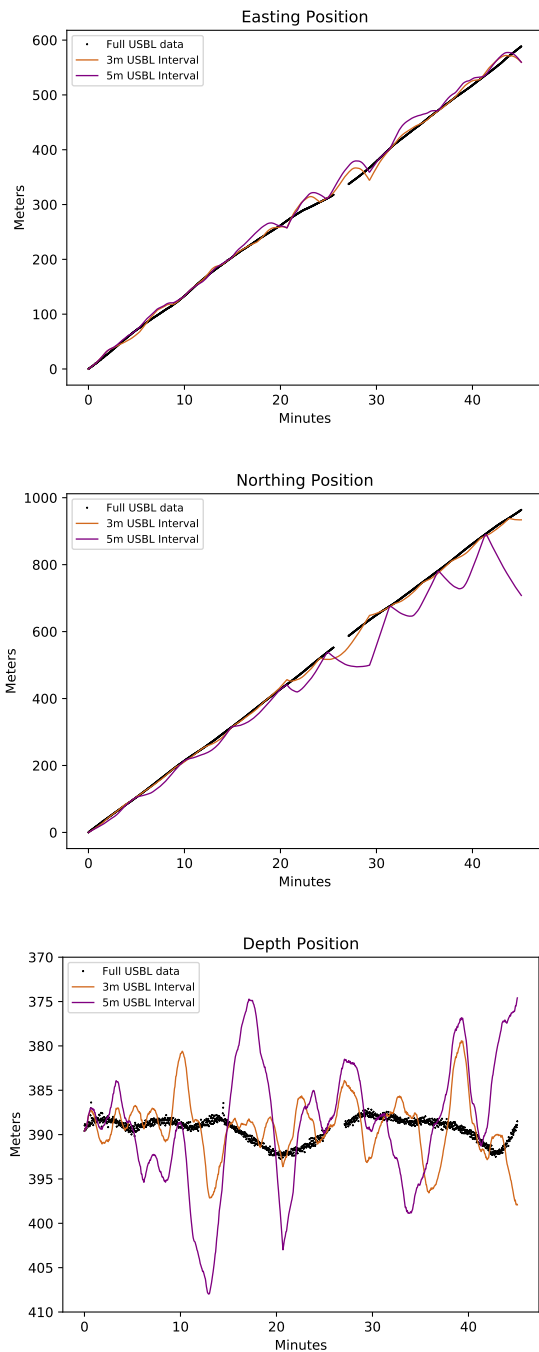


Fig. 13. Position fit over 50 minutes with 3 and 5 minute gaps in position data. With very low frequency of position data poor acceleration in the depth data leads to much less stable position estimates.

[2] B. D. O. Anderson and J. B. Moore. *Optimal Filtering*. Prentice Hall, 1979. 1, 2, 3

[3] C. F. Ansley and R. Kohn. A geometric derivation of the fixed interval smoothing algorithm. *Biometrika*, 69:486–487, 1982. 2

[4] A. Aravkin, J. V. Burke, L. Ljung, A. Lozano, and

G. Pillonetto. Generalized kalman smoothing: Modeling and algorithms. *Automatica*, 86:63–86, 2017. 2, 3, 7

[5] A. Y. Aravkin, J. V. Burke, and G. Pillonetto. Sparse/robust estimation and kalman smoothing with nonsmooth log-concave densities: Modeling, computation, and theory. *Journal of Machine Learning Research*, 14:2689–2728, 2013. 5

[6] F. Artacho and M. Geoffroy. Characterization of metric regularity of subdifferentials. *Journal of Convex Analysis*, 15(2):365–380, 2008. 6, 13

[7] Y. Bar-Shalom, X. R. Li, and T. Kirubarajan. *Estimation with Applications to Tracking and Navigation*. John Wiley and Sons, 2001. 3, 8

[8] Y. Bar-Shalom, X. Rong Li, and T. Kirubarajan. *Estimation with applications to tracking and navigation*. John Wiley & Sons, Inc., New York, 2001. 1

[9] B. M. Bell, J. V. Burke, and G. Pillonetto. An inequality constrained nonlinear Kalman-Bucy smoother by interior point likelihood maximization. *Automatica*, 45(1):25–33, Jan. 2008. 3

[10] P. L. Combettes and J.-C. Pesquet. Proximal splitting methods in signal processing. In *Fixed-point algorithms for inverse problems in science and engineering*, pages 185–212. Springer, 2011. 4, 5

[11] D. Davis and W. Yin. Convergence rate analysis of several splitting schemes. In *Splitting Methods in Communication, Imaging, Science, and Engineering*, pages 115–163. Springer, 2016. 4

[12] R. J. Hyndman, A. B. Koehler, R. D. Snyder, and S. Grose. A state space framework for automatic forecasting using exponential smoothing methods. *International Journal of Forecasting*, 18(3):439–454, 2002. 1

[13] A. Jazwinski. *Stochastic Processes and Filtering Theory*. Dover Publications, Inc, 1970. 3

[14] R. E. Kalman. A New Approach to Linear Filtering and Prediction Problems. *Transactions of the AMSE - Journal of Basic Engineering*, 82(D):35–45, 1960. 2

[15] P. Latafat, N. Freris, and P. Patrinos. A new randomized block-coordinate primal-dual proximal algorithm for distributed optimization. *arXiv preprint arXiv:1706.02882*, 2017. 5, 6

[16] L. Ljung. *System Identification - Theory for the User*. Prentice-Hall, Upper Saddle River, N.J., 2nd edition, 1999. 2

[17] H. Ohlsson, F. Gustafsson, L. Ljung, and S. Boyd. Smoothed state estimates under abrupt changes using sum-of-norms regularization. *Automatica*, 48:595–605, 2012. 3

[18] B. Oksendal. *Stochastic Differential Equations*. Springer, sixth edition, 2005. 3

[19] C. Paige. Computer solution and perturbation analysis of generalized linear least squares problems. *Mathematics of Computation*, 33:171–183, jan 1979. 2, 3

[20] H. E. Rauch, F. Tung, and C. T. Striebel. Maximum Likelihood estimates of linear dynamic systems. *AIAA J.*, 3(8):1145–1150, 1965. 2

[21] R. T. Rockafellar and R. J. B. Wets. *Variational Analysis*, volume 317. Springer, 1998. 5

[22] R. S. Tsay. *Analysis of financial time series*, volume 543. John Wiley & Sons, 2005. 1

Appendix

8.1 Proof of Theorem 3.1

Conditions 2, 3, 4 are easily seen to be equivalent. To see that 2 and 3 are equivalent, note that the matrix

$$\begin{bmatrix} Q_i^{1/2} & 0 \\ 0 & R_i^{1/2} \end{bmatrix}$$

is symmetric, so its nullspace is perpendicular to its range. Therefore surjectivity of D_i is equivalent to the

condition that the range of $\begin{bmatrix} I \\ H_i \end{bmatrix}$ covers this nullspace.

To see the equivalence of 2 and 4, recall that B is surjective if and only if BB^T is invertible, so D_i is surjective exactly when the matrix

$$\begin{bmatrix} Q_i + I & H_i^T \\ H_i & R_i + H_i H_i^T \end{bmatrix}$$

is invertible. $Q_i + I$ is always invertible, so invertibility of the block 2×2 matrix is equivalent to the invertibility of the Schur complement $R_i + H_i (I - (Q_i + I)^{-1}) H_i^T$. It remains to show that conditions 1 and 2 are equivalent. We proceed by induction on N . The base case is trivial, since for $N = 1$, $A = D_1$. For the inductive case, consider that for $N = k$ the result holds, and write the $N = k + 1$ case as

$$\begin{bmatrix} A_k & 0 \\ 0 & B_k \end{bmatrix} \begin{bmatrix} z_1 \\ z_2 \end{bmatrix} = \begin{bmatrix} w_1 \\ w_2 \end{bmatrix},$$

and assume that A_k is surjective. We then know that there exists z_1 that satisfies $A_k z_1 = w_1$. The second row can now be written explicitly as

$$D_{k+1} z_2 = w_2 + G_{k+1} x_k,$$

where x_k is the last component of z_1 . Thus A_{k+1} is surjective exactly when D_{k+1} is, as desired.

8.2 Proof of Lemma 4.2.

Proof: As D is monotone we have

$$\langle \eta^* - T\eta, D\eta^* - DT\eta \rangle \geq 0$$

as $0 \in (D + M)\eta^*$ this implies

$$\langle \eta^* - T\eta, -M\eta^* - DT\eta \rangle \geq 0$$

Now $DT\eta = DT\eta + HT\eta - HT\eta = (H - M)\eta - HT\eta$. Thus

$$\begin{aligned} 0 &\leq \langle \eta^* - T\eta, -M\eta^* + HT\eta - (H - M)\eta \rangle \\ &= \langle \eta^* - T\eta, -M(\eta^* - \eta) + H(T\eta - \eta) \rangle \\ &= \langle \eta^* - \eta, -M(\eta^* - \eta) + H(T\eta - \eta) \rangle \\ &\quad + \langle \eta - T\eta, -M(\eta^* - \eta) + H(T\eta - \eta) \rangle \end{aligned}$$

By definition of M we have

$$\langle M\eta, \eta \rangle = 0$$

for any η . Therefore

$$\begin{aligned} 0 &\leq \langle \eta^* - \eta, H(T\eta - \eta) \rangle + \langle \eta - T\eta, -M(\eta^* - \eta) \rangle \\ &\quad + \langle \eta - T\eta, H(T\eta - \eta) \rangle - \langle \eta - T\eta, M(T\eta - \eta) \rangle \\ &= \langle \eta^* - \eta, H(T\eta - \eta) \rangle + \langle \eta - T\eta, -M(\eta^* - \eta) \rangle - \|T\eta - \eta\|_{H-M}^2 \\ &= \langle \eta^* - \eta, H(T\eta - \eta) \rangle + \langle M(\eta - T\eta), \eta^* - \eta \rangle - \|T\eta - \eta\|_{H-M}^2 \\ &= \langle \eta^* - \eta, (H - M)(T\eta - \eta) \rangle - \|T\eta - \eta\|_{H-M}^2 \end{aligned}$$

8.3 Statement of [6], Theorem 3.3.

For a proper closed convex function f , the subdifferential ∂f is metrically subregular at \bar{x} for \bar{y} with $(\bar{x}, \bar{y}) \in \text{gra } \partial f$ if and only if there exists a positive constant c and a neighborhood \mathcal{U} of \bar{x} such that

$$f(x) \geq f(\bar{x}) + \langle \bar{y}, x - \bar{x} \rangle + cd^2(x, (\partial f)^{-1}(\bar{y})), \quad \forall x \in \mathcal{U}.$$

8.4 Computing with Prox Operators

In this section, we collect the proximal operators used in the paper. From simple calculus, we have

- $\text{prox}_{\frac{\gamma}{2}\|\cdot\|^2}(z) = \frac{1}{1+\gamma}z$.

This generalizes to easily invertible least squares terms:

- $\text{prox}_{\alpha\frac{1}{2}\|Ax-b\|^2}(z) = (I + \alpha A^T A)^{-1}(\alpha A^T b + z)$.

For $\rho(z) = \delta_C(z)$, we have

$$\text{prox}_{\gamma\rho}(z) = \text{proj}_C(z).$$

This gives simple formulas for the following operators:

- $\text{proj}_{\gamma\mathbb{B}_2}(z) = \min(\|z\|, \gamma) \frac{z}{\|z\|}$.

- $\text{proj}_{\gamma\mathbb{B}_\infty}(z) = \min(\max(z, -\gamma), \gamma)$.
- $\text{proj}_{\mathbb{R}_+}(z) = \max(z, 0)$.

We also have fast implementations for the following operators:

- $\text{proj}_{\gamma\mathbb{B}_1}(z)$, the 1-norm projection
- $\text{proj}_{\gamma\Delta}(z)$, the scaled simplex projection
- $\text{proj}_{\gamma\Delta_1}(z)$, the capped simplex projection.

Next, the Moreau identity relates the prox operators for f and f^* :

$$\text{prox}_{\alpha f^*}(z) = z - \alpha \text{prox}_{\alpha^{-1}}(\alpha^{-1}z)$$

This identity together with previous results yields the following operators:

- $\text{prox}_{\gamma\|\cdot\|_2}(z)$
- $\text{prox}_{\gamma\|\cdot\|_1}(z)$
- $\text{prox}_{\rho_h}(z)$, prox of hinge loss.
- $\text{prox}_{\gamma\|\cdot\|_\infty}$

Often we add a simple quadratic to a penalty; the prox of the sum can be expressed in terms of the prox of the original penalty.

- $\text{prox}_{\alpha(f+\gamma/2\|\cdot\|^2)}(x) = \text{prox}_{\frac{\alpha}{1+2\alpha\gamma}f}\left(\frac{1}{1+2\alpha\gamma}x\right)$.

This immediately gives the prox of the elastic net, which is the sum of the 1-norm and a simple quadratic.

Likewise, we can compute the prox of a Moreau envelope of a given penalty.

- $\text{prox}_{\gamma e_{\alpha\rho}}(z) = \frac{\alpha}{\gamma+\alpha}z + \frac{\gamma}{\gamma+\alpha}\text{prox}_{(\gamma+\alpha)\rho}(z)$

This immediately gives us formulas for prox of the Huber, as well as smoothed variants of any other penalty in the collection.